Journal of Materials Chemistry C

Accepted Manuscript

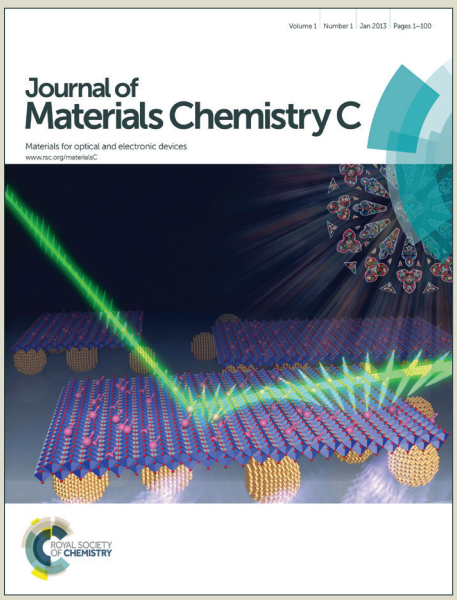

ROYAL SOCIETY OF CHEMISTRY

www.rsc.org/materialsC

Local charge writing in epitaxial $SmNiO_3$ thin films

Feng Yan*, †, Frank Schoofs†, Jian Shi†, Sieu D. Ha, R. Jaramillo, and Shriram Ramanathan

School of Engineering and Applied Sciences, Harvard University, Cambridge, Massachusetts 02138, USA

†These authors contributed equally to this work.

ABSTRACT

We have investigated the evolution of work function in epitaxial correlated perovskite $SmNiO_3$ (SNO) thin film spanning the metal-insulator transition (MIT) by Kelvin probe force microscopy (KPFM). Combining contact-mode atomic force microscopy, KPFM and electrostatic force microscopy (EFM), we present charge writing processes associated with point defect engineering in the SNO thin films. Surface potential tuning in two-terminal devices is demonstrated and compared to thermal control by proximity to the phase transition boundary. The charge distribution, retention, and diffusion on SNO were systematically examined. Local compositional changes by AFM-tip induced electric fields is shown to be a viable approach to spatially engineer electronic properties of correlated oxides towards eventual applications in electronics.

KEYWORDS: Nickelate, Kelvin probe force microscopy, Metal-insulator transition, charge writing, memory, phase change.

* fengyan@seas.harvard.edu

Introduction

Rare earth nickelates $RNiO_3$ (R is rare-earth element, e.g. Pr, Nd, or Sm) exhibiting temperature-driven metal-insulator transitions (MIT) are of interest in fundamental condensed matter studies towards understanding electronic phase diagrams in correlated electron systems and for emerging electron devices. Samarium nickelate is of particular interest owing to its electronic phase transition near 403 K that is above junction temperature of typical electronic circuits.[1-3] The thermodynamic instability of some of the nickelate semiconductors such as $SmNiO_3$ however places severe restrictions on growth parameters and requires great care. [4-8] Epitaxial films can be stabilized using substrate-imposed strain and with appropriate compositional control during growth or post-annealing one can realize fully reversible phase transitions. Such reversible transitions allow reproducible measurements of various properties and allow further detailed studies on the intrinsic material properties. Studies on electronic properties on thin films of such perovskite nickelates are in nascent stages ranging from determination of fundamental physical properties to proof-of-concept solid-state devices. Parameters well known for traditional semiconductors such as band gap, work function, dielectric properties are often lacking for such correlated materials and are crucial to advance understanding the band structure and response to external fields. Scanning probe microscopy (SPM) technologies with high spatial resolution are well suited to characterize electronic properties of semiconductors. [9-12] For example, Kelvin probe force microscopy (KPFM) has been used to characterize charge

distribution within oxides,[13-16] and electrostatic force microscopy (EFM) has been utilized to determine trapping phenomena in oxide surfaces/interfaces.[17-22]

Using a conducting-tip atomic force microscope (AFM) one has the ability to manipulate electric charge on oxides, so as to realize the write, erase and read operation potentially pertinent to memory devices.[23-29] High local fields such as generated with the AFM can also be used to change near-surface composition of oxides leading to non-volatile changes in their conduction properties.[30-38] Here we report measurements of temperature/voltage dependence of work function of $SmNiO_3$ (SNO) across the electronic phase transition. By a combination of contact-mode atomic force microscopy (AFM), electrostatic force microscopy (EFM) and KPFM, we demonstrate switchable charge writing behavior in SNO by local defects and further characterize the charge distribution, and subsequent charge diffusion and retention features.

Experimental

Materials Synthesis and structural characterization: Epitaxial SNO films were prepared by RF magnetron sputtering in high background pressure (265 mTorr) from a stoichiometric target onto (001)-oriented single crystal $LaAlO_3$ (LAO) substrates. The epitaxial SNO films were also successfully fabricated using magnetron co-sputtering from metallic Sm and Ni targets, followed by a 100 bar O_2 and 500 ^oC annealing for 24 hours. X-ray diffraction (XRD) spectra and transmission electron microscopy (TEM) images of samples were conducted to examine the epitaxial growth and phase purity.

Scanning microscopy and calibration: KPFM and EFM measurements were carried out using a commercial atomic force microscope (AFM, Asylum Research, MFP-3D) with a conducting tip (Olympus, AC240TM) in air. The work function of the conductive tips (~4.90 eV) was calibrated with freshly cleaved highly oriented pyrolytic graphite (HOPG, Grade-1 SPI, ~4.65 eV). This is a commonly used approach to obtain reference values for work function determination of functional materials.[39] For charge writing, the AFM was operated in contact mode, deflection set point (0.2 V), scan rate 0.5 Hz, and spring constant of the tip (~ 2 N/m). For characterization of work function, the KPFM mode with tapping amplitude was set to be ~500 mV at low temperature and ~100 mV at higher temperature. EFM characterization was performed with reading voltage at both positive and negative dc bias 3 V. For analysis of the surface potential and phase variation in the written areas, the surface potential and electrostatic phase images were flattened by a first order polynomial. [40, 41] The tip lift height is about 30 nm for both KPFM and EFM measurements. All scanning probe microscopy measurements have been conducted on the epitaxial SNO samples co-sputtered from Ni and Sm targets and grown from SNO single target, respectively, similar behavior were achieved. In order to minimize the possible water adsorbates, the SNO films were annealed at 423 K for 30 min prior to the KPFM measurement. [42]

Results and Discussion

The temperature dependent resistance of the grown SNO was examined and the metal-insulator transition temperature is determined at 403±1 K (Fig. 1a). Figure

1b-c shows the high-resolution X-ray diffraction (XRD) spectrum and the two-dimensional-XRD (2D-XRD) for a 55 nm thick SNO, respectively, with growth of oriented (110) SNO on 001-oriented $LaAlO_3$ (LAO) single crystal substrate. The high-resolution diffraction (Fig. 1b) identifies that the (110) plane of the SNO is parallel to the LAO (001), which is consistent with the epitaxial relationship between LAO and SNO thin film synthesized by other methods. [6, 43] The two-dimensional X-ray diffractogram exhibits distinct diffraction spots related to the SNO crystal structure, as indicated in Fig. 1c. This indicates epitaxial orientation of the SNO thin film on the LAO, demonstrating the powerfulness of such solid phase epitaxy growth method. High-resolution TEM (HRTEM) and electron diffraction pattern analysis identifies and supports the epitaxial orientation of the (110)-SNO parallel to (001)-LAO (Fig. 1d). (The diffraction patterns of SNO and LAO were obtained from the same TEM sample in the absence of either sample or beam tilting). Local epitaxial relationships from Fast Fourier transformation (FFT) patterns are also found to be consistent with the result acquired from both XRD and electron diffraction patterns.

To characterize the electronic phase transition spanning the MIT of the SNO films, we measured the local work function (Φ) by Kelvin Probe force microscopy (KPFM) while varying the sample temperature. KPFM measures the contact potential difference (ΔCPD) between the conductive tip (Φ_{tip}) and the sample (Φ_{sample}), i.e., $\Delta \mathrm{CPD} = (\Phi_{tip} - \Phi_{sample})/e$. Calibration is an important step for the KPFM measurements to obtain quantitative information on electronic properties. Here,

freshly cleaved highly oriented pyrolytic graphite (HOPG, SPI Grade I) was used as a reference sample to calibrate the work function of KPFM probes, since the work function of HOPG is well-documented and stable (4.65 eV). [44] We performed the KPFM measurement on HOPG and the work function of the tips used for KPFM were determined to be ~(4.90±0.02) eV according to $\Phi_{tip} = e\Delta\mathrm{CPD}_{\mathrm{HOPG}} + \Phi_{HOPG}$.

The AFM image of SNO in Fig. 2a shows that our films are continuous with root mean square roughness ~0.4 nm. KPFM images were recorded during heating the sample in steps of ~10 K, and the system was kept at the selected temperature for 30 min to achieve thermal equilibrium before measuring. The cantilever was re-tuned at each step to keep in the vicinity of the resonance frequency, and lateral offsets were adjusted to a fixed topographical feature to eliminate thermal drift. Figure 2b-c indicates a series of surface potential images obtained by scanning at various temperatures. The average contact potential difference increased with increasing temperature, and the corresponding calculated work function decreased from 4.93 ± 0.02 eV at 300 K to 4.79 ± 0.02 eV at 443 K (Fig. 2d). The temperature dependence of work function displays a smooth transition behavior cross the phase transition temperature, which can be ascribed to the extremely narrow bandgap of SNO at insulating phase (band gap of the order of fraction of an eV). [45]

We then tune the surface potential of SNO under electrical excitation and characterize using KPFM in a two-terminal device. Pt top electrodes were sputtered by photo-lithographic patterning with thickness about 100 nm, as shown in Fig. 3a.

The driven voltage for the phase transition is in the vicinity of 0.5 V for the device with Width/Length (W/L) = 160/10 μm. Figure 3b shows the KPFM images of SNO with bias voltages applied at one electrode at 0V, +0.5V, and -0.5V, while the other electrode was grounded. The CPD change can be observed clearly. The biased electrode shifts upward (downward) as external voltage increases (decreases). From the CPD profiles referenced to the grounded electrode (Fig. 3c), linear variation of CPD in the SNO channel can be obtained. The CPD profiles at different bias voltage are modified about 0.10 eV in SNO. The linear potential drop across the SNO film is a fraction of the applied bias and can be ascribed to the parallel capacitance contributions from the neighboring electrodes, which leads to a smaller potential drop in the applied bias. [46, 47] Note that the temperature-induced change of work function is 0.14 ± 0.02 eV from the metal phase at 443 K to the insulating phase at 300 K (Fig. 2d), consistent with voltage-induced transition.

To characterize charge retention in the insulating phase, we perform charge writing on the surface of SNO at room temperature. Our primary results are shown in Fig. 4, where the combination of KPFM and EFM analysis of the SNO film subjected to writing by positive (outside) and negative (inside) bias voltage (±1 V) with a conducting tip by contact-mode AFM. Figure 4a-b shows the KPFM images prior to and after the charge writing process, respectively. The measured surface potential (lift height ~30 nm) of the written area at opposite bias voltages (Fig. 4b) indicates a switchable charge writing behavior, and positive bias leads to a positive potential (outside), while negative bias gives a negative potential (inside). To confirm the

switchable character of these charges, EFM experiments were performed at the same regions. The EFM images of the produced patterns obtained with a dc read voltage of -3 and +3 V (Fig. 4c and 4d), respectively, and show inverted contrast. In EFM images achieved by -3 V read voltage (Fig. 4c), dark areas under the application of the negative bias (-1 V), correspond to a negative surface charge, which is due to the fact that repulsive force leads to a decrease in phase. In contrast, the bright areas (written by positive bias, Fig. 4c) correspond to positive surface charge due to the attractive force resulting in gain in phase. The counterpart phase images are recorded in the EFM image obtained by +3 V read voltage (Fig. 4d).

Next we focus on the electrochemical mechanism of this writing process, which is illustrated in the schematic diagrams in Fig. 4e. Ambient effects on the local charge on SNO are also considered because it has significant impact on the charge modification. [48-50] In the case of insulating SNO, there exists a contribution from charge distribution to the surface dipoles (i.e. oxygen ions O_2^-, O^{2-}), oxygen vacancies ($V_O^{\bullet\bullet}$), holes ($h^{\bullet}$) and electrons (e^-) (Fig. 4e). The biased tip can desorb surface adatoms and dissociate surface atoms, and the removal of oxygen from the SNO surface can be achieved using a positive biased tip (i.e. 1i: the virgin film, 1ii: field-induced redox reaction, and 1iii: generate oxygen vacancies. [50]) and recovery with negative bias. [48] From the potential profile for the as-written areas (Fig. 4d), the contact potential differences reflect the back and forth change in electronic nature of the written area under opposite bias. The contact potential difference in the central region written with negative bias is much larger (absolute value) than

those of the positive one. To further ascertain the switchable charge writing behavior, various dc biases were performed at the same area. Figure 4f-g display the contact potential difference and corresponding CPD profile, indicating that the written area can be erased.

To determine the durability of the charges, we performed a series of experiments on the charge written areas to characterize the local charge retention behavior in "discharge process", time and temperature, as shown in Fig. 5. First, we applied a "discharge process" for the written area with a grounded conductive tip in the contact mode, where the grounded tip can sweep the surface charges due to the potential difference between ground and the film surface. [51] As shown in Fig. 5a, the reduction of the surface charge in the discharged area is clearly seen compared with the as-written one (Figure 4b), and the corresponding quantified potential profile is shown in Figure 5d, confirming the charge transfer from the surface to the grounded tip.

Figure 5b displays the KPFM image of the written features after 4 hours, where the charges decreased due to relaxation. [52] The corresponding potential profile in Figure 4d indicated that the decay time to equilibrium value is on the order of hours. To quantitatively examine the surface charge retention behavior, we performed charge-writing processes at a higher bias for different areas (i.e. ± 3 V, inset of Figure 5e) and plotted the average surface potential as a function of time (Figure 5e). The potential can be well fit by exponential decay (solid lines) of the form

$p(t) = p_0 + p_1 \exp(-t/\tau)$, where t is the time, p_0 is the asymptotic equilibrium value of the potential, and τ is the characteristic time of charges. The characteristic time τ is ~4000 s for both cases as shown in Table 1. This characteristic time is of the same order of magnitude as that reported for perovskite interfaces (~2000 s). [22] Additional measurements to determine the charge dynamics utilizing temperature variation were then carried out. Figure 5c shows the KPFM image for the written area upon heating to 348 K for 30 min (below the MIT temperature to rule out the phase transition effect). The contact potential difference for the written area became weak after heating, corresponding to the profile in Figure 5d.

To investigate the surface charge behavior spanning the metal-insulator transition, we increased the stage temperature and recorded the KPFM images to the transition temperature for one positive charged area (+1 V), as shown in Fig. 6a-c. Figure 6d shows the contact potential difference profiles achieved from the KPFM images reduce greatly, suggests that increasing the temperature can accelerate the charge decay and higher temperature can accelerate the relaxation processes. With increasing temperature, the metallic nuclei appear in the insulating matrix, where the charge transfer gap decreases. In other words, the conduction band and valence band overlap during the metal insulator transition; the stored charges will be reduced. Similar behavior was seen in the negatively charged area. We further determine the bias dependence of the written charges on the SNO surface. Figure 7a shows KPFM image acquired from a 7×7 μm^2 region, where eleven 3×0.27 μm^2 rectangular regions were written from +3V (top) to -3V (bottom) in a 0.6 V step in

contact mode. The corresponding line profile is shown in Fig. 7d, a strong asymmetry and continuous variation in the potential distribution can be observed; positive dc bias gained weaker potential differences than that of negative dc bias. The EFM phase images of the same location obtained with a dc read voltage of +3V and -3V were shown in Figures 7b and 7c respectively. Figure 7e shows the bias dependence of the corresponding EFM phase profiles, where a stepwise decrease of bias voltage results in a sharp transition between the biased regions and the virgin SNO. These results suggest that different bias voltages tune the degree of the electrochemical processes on the SNO surface and allow control of the local electronic properties.

Conclusions

We have experimentally determined the temperature dependence of work function across insulator-metal transition in epitaxial samarium nickelate using Kelvin probe force microscopy (KPFM). Charge writing in SNO at nanoscale via a combination of contact-mode AFM, KPFM and EFM is studied quantitatively. The ability to locally store and read information in such nickelates has potential relevance to the growing interest in exploring correlated electron systems for electronics.

Acknowledgement.

The authors acknowledge financial support from National Science Foundation, AFOSR, National Academy of Sciences and ARO MURI.

References

1. F. Conchon, A. Boulle, C. Girardot, S. Pignard, R. Guinebretière, E. Dooryhée, J. L. Hodeau, F. Weiss, J. Kreisel and J. F. Bérar, *J. Phys. D: Appl. Phys.*, 2007, **40**, 4872.
2. S. D. Ha, G. H. Aydogdu and S. Ramanathan, *J. Appl. Phys.*, 2011, **110**, 094102-094105.
3. M. A. Mroginski, N. E. Massa, H. Salva, J. A. Alonso and M. J. Martínez-Lope, *Phys. Rev. B*, 1999, **60**, 5304-5311.
4. N. Ihzaz, S. Pignard, J. Kreisel, H. Vincent, J. Marcus, J. Dhahri and M. Oumezzine, *Phys. Status Solidi (c)*, 2004, **1**, 1679-1682.
5. G. H. Aydogdu, S. D. Ha, B. Viswanath and S. Ramanathan, *J. Appl. Phys.*, 2011, **109**, 124110.
6. N. Ihzaz, M. Oumezzine, J. Kreisel, H. Vincent and S. Pignard, *Chem. Vap. Deposition*, 2008, **14**, 111-114.
7. M. A. Novojilov, O. Y. Gorbenko, I. E. Graboy, A. R. Kaul, H. W. Zandbergen, N. A. Babushkina and L. M. Belova, *Appl. Phys. Lett.*, 2000, **76**, 2041-2043.
8. F. Conchon, A. Boulle, R. Guinebretière, E. Dooryhée, J. L. Hodeau, C. Girardot, S. Pignard, J. Kreisel and F. Weiss, *J. Phys.: Condens. Matt.*, 2008, **20**, 145216.
9. M. Nonnenmacher, M. P. O'Boyle and H. K. Wickramasinghe, *Appl. Phys. Lett.*, 1991, **58**, 2921-2923.
10. H. O. Jacobs, P. Leuchtmann, O. J. Homan and A. Stemmer, *J. Appl. Phys.*, 1998, **84**, 1168-1173.
11. H.-J. Butt, B. Cappella and M. Kappl, *Surf. Sci. Rep.*, 2005, **59**, 1-152.
12. M. H. Lee and C. S. Hwang, *Nanoscale*, 2011, **3**, 490-502.
13. J. Y. Son, B. G. Kim, C. H. Kim and J. H. Cho, *Appl. Phys. Lett.*, 2004, **84**, 4971-4973.
14. J. Y. Son, S. H. Bang and J. H. Cho, *Appl. Phys. Lett.*, 2003, **82**, 3505-3507.
15. G. H. Enevoldsen, T. Glatzel, M. C. Christensen, J. V. Lauritsen and F. Besenbacher, *Phys. Rev. Lett.*, 2008, **100**, 236104.
16. X. M. Lu, F. Schlaphof, S. Grafström, C. Loppacher, L. M. Eng, G. Suchaneck and G. Gerlach, *Appl. Phys. Lett.*, 2002, **81**, 3215-3217.
17. G. H. Buh, H. J. Chung and Y. Kuk, *Appl. Phys. Lett.*, 2001, **79**, 2010-2012.
18. J. T. Jones, P. M. Bridger, O. J. Marsh and T. C. McGill, *Appl. Phys. Lett.*, 1999, **75**, 1326-1328.
19. S. V. Kalinin and D. A. Bonnell, *Nano Lett.*, 2004, **4**, 555-560.
20. P. Lehnen, J. Dec and W. Kleemann, *J. Phys. D: Appl. Phys.*, 2000, **33**, 1932.
21. P. Girard, *Nanotechnology*, 2001, **12**, 485.
22. Y. Xie, C. Bell, T. Yajima, Y. Hikita and H. Y. Hwang, *Nano Lett.*, 2010, **10**, 2588-2591.
23. W. M. D. Wright and D. G. Chetwynd, *Nanotechnology*, 1998, **9**, 133.
24. P. Mesquida, H. F. Knapp and A. Stemmer, *Surf. Interface Anal.*, 2002, **33**, 159-162.
25. J. E. Stern, B. D. Terris, H. J. Mamin and D. Rugar, *Appl. Phys. Lett.*, 1988, **53**, 2717-2719.

26. C. H. Ahn, T. Tybell, L. Antognazza, K. Char, R. H. Hammond, M. R. Beasley, Ø. Fischer and J.-M. Triscone, *Science*, 1997, **276**, 1100-1103.
27. L. M. Eng, M. B. C. Loppacher, M. G. R. Bennewitz, R. Lüthi, E. M. T. Huser, H. Heinzelmann and H. J. Güntherodt, *Ferroelectrics*, 1999, **222**, 153-162.
28. J. W. Hong, D. S. Kahng, J. C. Shin, H. J. Kim and Z. G. Khim, *J. Vac. Sci. Technol. B*, 1998, **16**, 2942-2946.
29. E. B. Cooper, S. R. Manalis, H. Fang, H. Dai, K. Matsumoto, S. C. Minne, T. Hunt and C. F. Quate, *Appl. Phys. Lett.*, 1999, **75**, 3566-3568.
30. S. K. R. S. Sankaranarayanan, E. Kaxiras and S. Ramanathan, *Energy Environ. Sci.*, 2009, **2**, 1196-1204.
31. X. N. Xie, H. J. Chung, C. H. Sow and A. T. S. Wee, *Mater. Sci. Eng. R: Rep.*, 2006, **54**, 1-48.
32. S. Gwo, C.-L. Yeh, P.-F. Chen, Y.-C. Chou, T. T. Chen, T.-S. Chao, S.-F. Hu and T.-Y. Huang, *Appl. Phys. Lett.*, 1999, **74**, 1090-1092.
33. P. Avouris, R. Martel, T. Hertel and R. Sandstrom, *Appl. Phys. A*, 1998, **66**, S659-S667.
34. D. Stiévenard, P. A. Fontaine and E. Dubois, *Appl. Phys. Lett.*, 1997, **70**, 3272-3274.
35. B. Legrand and D. Stievenard, *Appl. Phys. Lett.*, 1999, **74**, 4049-4051.
36. Y. Okada, S. Amano, M. Kawabe and J. S. Harris, *J. Appl. Phys.*, 1998, **83**, 7998-8001.
37. A. Kumar, F. Ciucci, A. N. Morozovska, S. V. Kalinin and S. Jesse, *Nat. Chem.*, 2011, **3**, 707-713.
38. R. Garcia, R. V. Martinez and J. Martinez, *Chem. Soc. Rev.*, 2006, **35**, 29-38.
39. V. Palermo, S. Morelli, M. Palma, C. Simpson, F. Nolde, A. Herrmann, K. Müllen and P. Samorì, *ChemPhysChem*, 2006, **7**, 847-853.
40. R. Jaramillo and S. Ramanathan, *Adv. Funct. Mater.*, 2011, **21**, 4068-4072.
41. S. Guo, S. V. Kalinin and S. Jesse, *Nanotechnology*, 2012, **23**, 125704.
42. H. Sugimura, Y. Ishida, K. Hayashi, O. Takai and N. Nakagiri, *Appl. Phys. Lett.*, 2002, **80**, 1459-1461.
43. F. Conchon, A. Boulle, R. Guinebretière, C. Girardot, S. Pignard, J. Kreisel, F. Weiss, E. Dooryhée and J.-L. Hodeau, *Appl. Phys. Lett.*, 2007, **91**, 192110.
44. M. Palma, J. Levin, V. Lemaur, A. Liscio, V. Palermo, J. Cornil, Y. Geerts, M. Lehmann and P. Samorì, *Adv. Mater.*, 2006, **18**, 3313-3317.
45. S. D. Ha, R. Jaramillo, D. M. Silevitch, F. Schoofs, K. Kerman, J. D. Baniecki and S. Ramanathan, *Phys. Rev. B*, 2013, **87**, 125150.
46. R. Baier, C. Leendertz, M. C. Lux-Steiner and S. Sadewasser, *Phys. Rev. B*, 2012, **85**, 165436.
47. J. Q. Nathaniel, N. S. Robert, B. Sung-Soo and R. Regina, *Nanotechnology*, 2013, **24**, 205704.
48. D. Li, M. H. Zhao, J. Garra, A. M. Kolpak, A. M. Rappe, D. A. Bonnell and J. M. Vohs, *Nat Mater*, 2008, **7**, 473-477.
49. S. Sadewasser and C. Barth, in *Characterization of Materials*, John Wiley & Sons, Inc., 2002.
50. H. Kim, S. Hong and D.-W. Kim, *Appl. Phys. Lett.*, 2012, **100**, 022901-022904.

51. J. Y. Son, K. Kyhm and J. H. Cho, *Appl. Phys. Lett.*, 2006, **89**, 092907-092903.
52. S. H. Lee, M. Kim, S. D. Ha, J.-W. Lee, S. Ramanathan and S. Tiwari, *Appl. Phys. Lett.*, 2013, **102**, 072102-072104.

Table

Table 1. The fitting parameters of the solid curves shown in Figure 5e of the main text, in the form of $p(t) = p_0 + p_1 \exp(-t/\tau)$

Bias voltage (V)	p_0 (mV)	p_1 (mV)	τ (min)
+3	2.49±0.12	4.08±0.26	70.4±1.03
-3	-128.5±1.59	-44.89±3.73	63.3±1.15

p_0 for V_{write} >0 is about 37 % of $p(t=0)$, and p_0 for V_{write} <0 is about 73 % of $p(t=0)$, demonstrating stability (>20 hours).

Figure Captions

Fig. 1. (a) Temperature dependent resistance for epitaxial SNO thin film. (b) High resolution XRD around the LAO (002) peak for the co-sputtered SNO thin films. (c) Two-dimensional XRD images of co-sputtered SNO. The horizontal 2θ axis runs from 16^o to 52^o in the center of the images, with equi-angle semi-circles across different χ ($\sim 30^o$ in vertical direction). (d) High resolution (HRTEM) images and selected area electron diffraction (SAED) of 110-oriented SNO on 001-oriented LAO substrate. Inset in (d) shows the SNO/LAO interfacial structure at atomic resolution. Dashed line indicates the position of the interface.

Fig. 2. (a) AFM topography (5×5 μm^2) of $SmNiO_3$ film on $LaAlO_3$ substrate and (b) corresponding KPFM images at 300 K. (c) KPFM images (2×5 μm^2) taken at various temperatures spanning the electronic phase transition. (d) Contact potential difference (CPD, left axis) with respect to temperatures and corresponding calculated local work function (right axis).

Fig. 3 (a) Optical image of SNO channel with W/L = 160/10 μm used to measure voltage dependent CPD. (b) KPFM images (20×20 μm^2) under different bias voltage. (c) CPD profiles under different bias voltage referenced to the grounded electrode.

Fig. 4. (a, b) KPFM images (5×5 μm^2) taken prior to (virgin state) and after charge writing process. Frames written in the contact mode by scanning the SNO surface with the KPFM probe under opposite dc bias voltages, V_{write} = +1 V (outside) and -1 V (inside.). (c, d) EFM phase images (5×5 μm^2) taken at the same area as the KPFM images. The EFM images were acquired with a dc read voltage of (b)-3 V and (c)+3 V. Here, locations of bright contrast represent upward oriented charges and correspond to a positive surface charge, as shown in (c), and inversely in (d). (e) Schematic diagrams for the possible mechanism during charge writing on the SNO surface before (1i) and during the charge writing (1ii. desorb oxygen anions, 1iii. oxygen vacancies generation, and 2. different bias voltage on tip) in air. (f) KPFM images (15 × 15 μm^2) based on switchable charge writing in SNO: +1V: 8×8 μm^2, -1V: 6×6 μm^2, +2V: 4×4 μm^2; -2V: 2×2 μm^2. (g) Corresponding contact potential difference line profile for the written/erased area.

Fig. 5. KPFM images (5×5 μm^2) of ± 1 V written area taken after (a) discharge process using grounded conductive tip, (b) relaxing 4 hours after writing and (c) heating up to 348 K, respectively. (d) Corresponding contact potential difference (ΔCPD) line profiles for the written area under various processes to ascertain the durability of the written charges. (e) Time-dependence of the average potential of the written features (V_{write} = ± 3 V). Inset shows the corresponding KPFM image acquired at different written area.

Fig. 6. KPFM images (7×7 μm^2) recorded at +1 V written area (slashed box, 5×5 μm^2) at (a) 300 K, (b) 348 K and (c) 403 K. (d) corresponding CPD profiles for the written area at various temperatures.

Fig. 7. (a) KPFM image (7×7 μm^2) after writing using varying V_{write} from +3 V (top) to -3 V (bottom) with ΔV = 0.6 V. Arrow indicates the scan direction. (b, c) EFM phase images taken at the same written patterns as the KPFM images, read with a dc voltage, (b) V_{read} = +3 V and (c) V_{read} = -3 V, respectively. (d) Contact potential difference (ΔCPD) line profile across KPFM image (a), as indicated by white dash line in (a). (e) Line profile across EFM phase images (b, c). The arrow in scan direction and the ΔV is the applied bias voltage step.

Figures

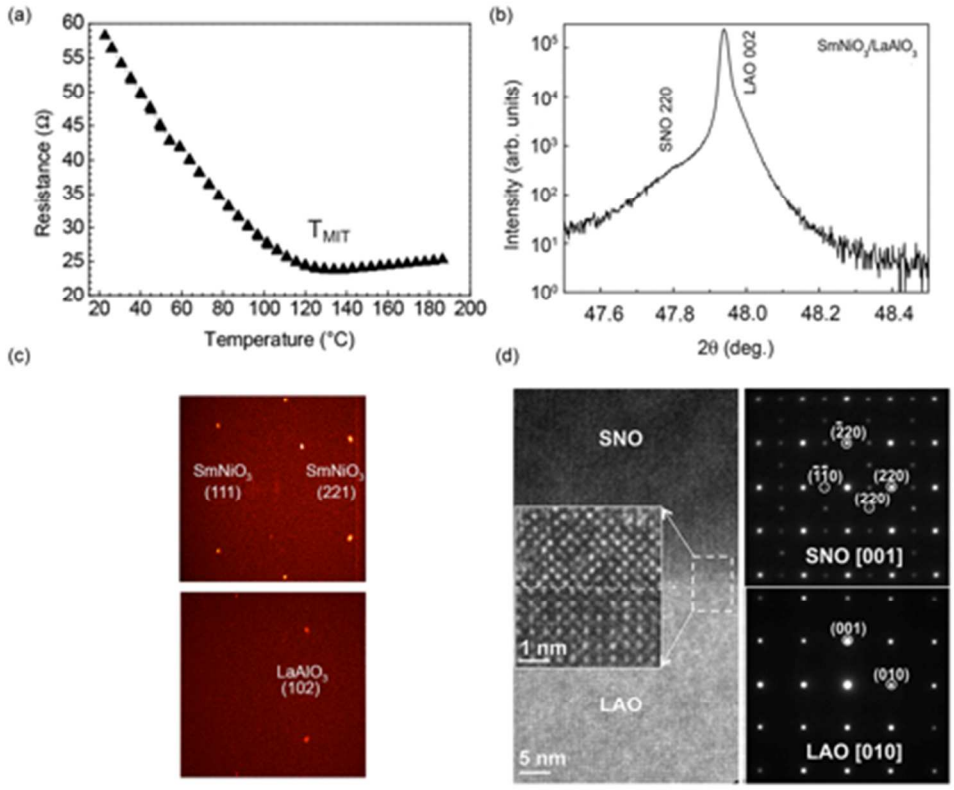

Fig. 1

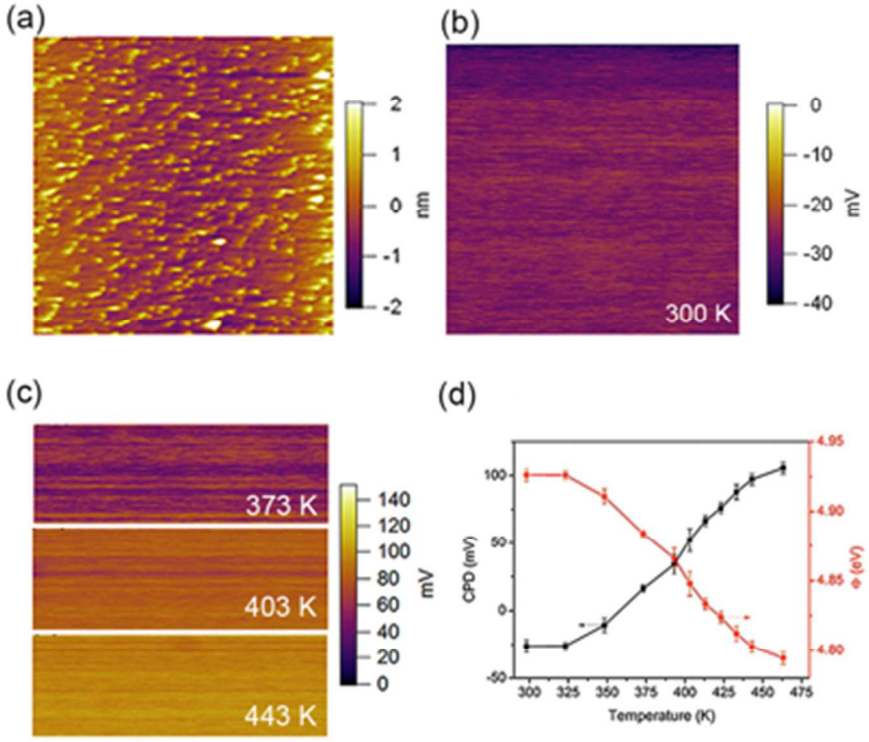

Fig. 2

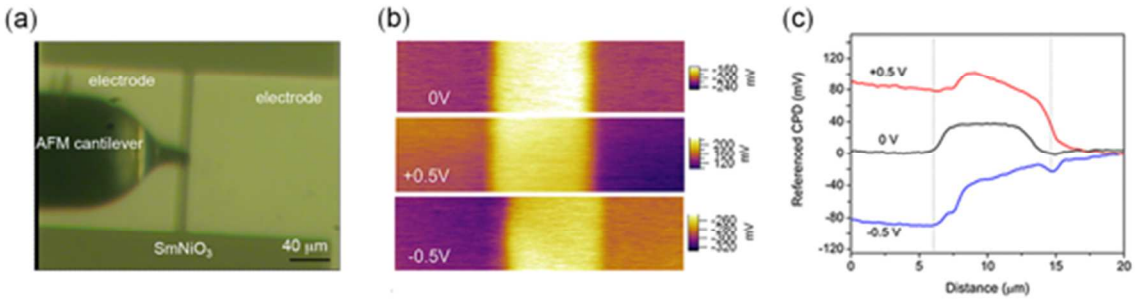

Fig. 3

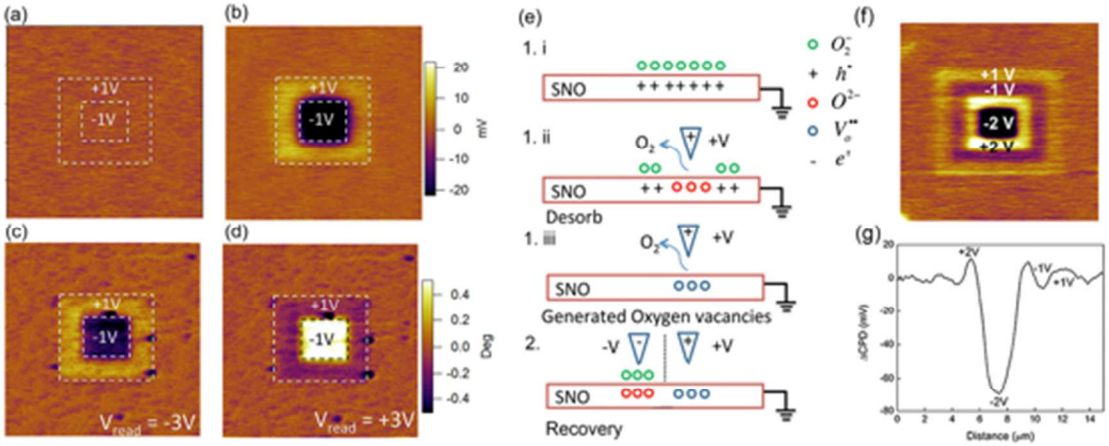

Fig. 4

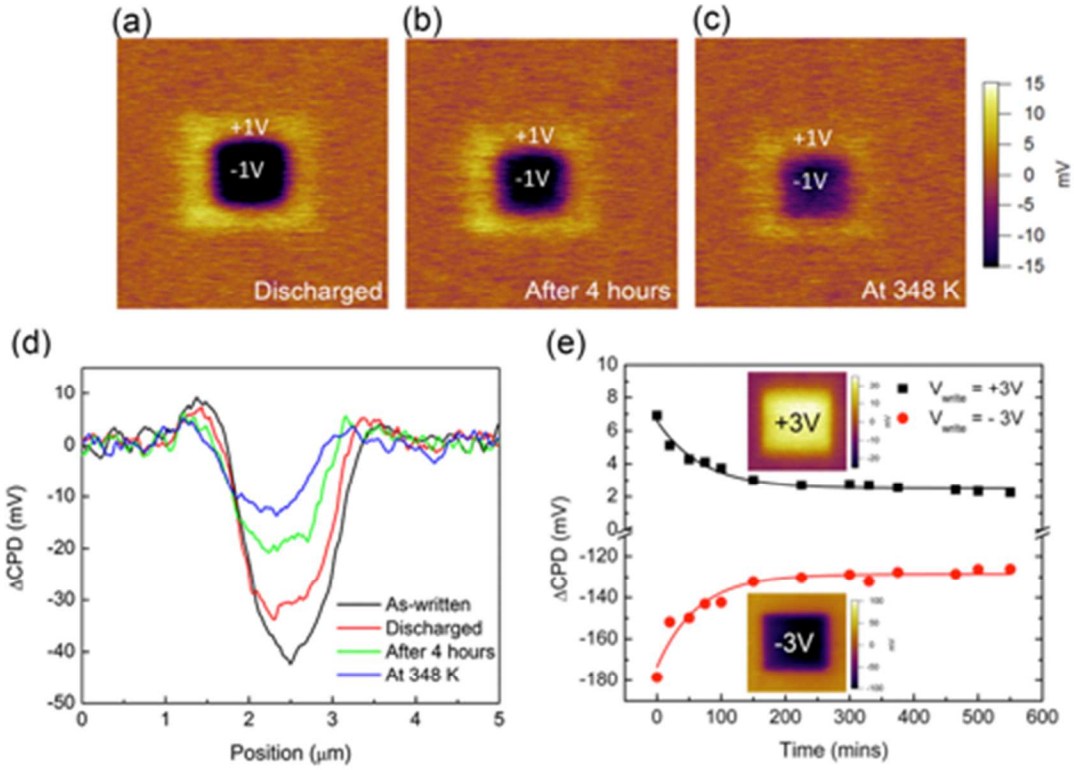

Fig. 5

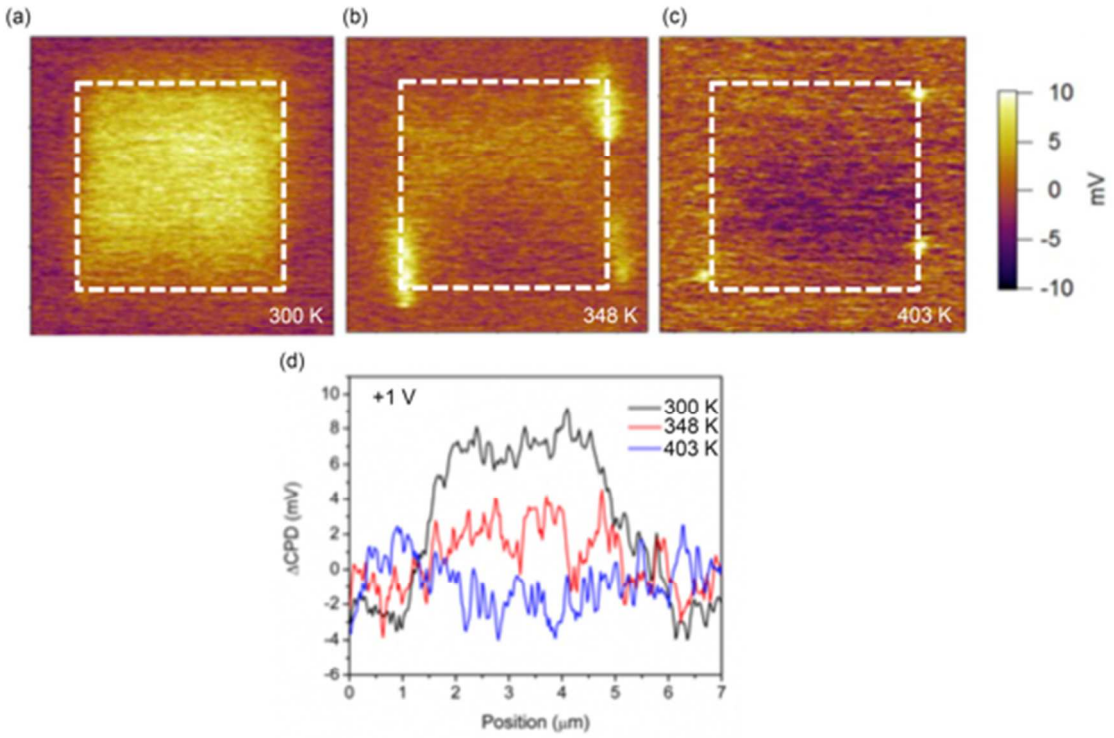

Fig. 6

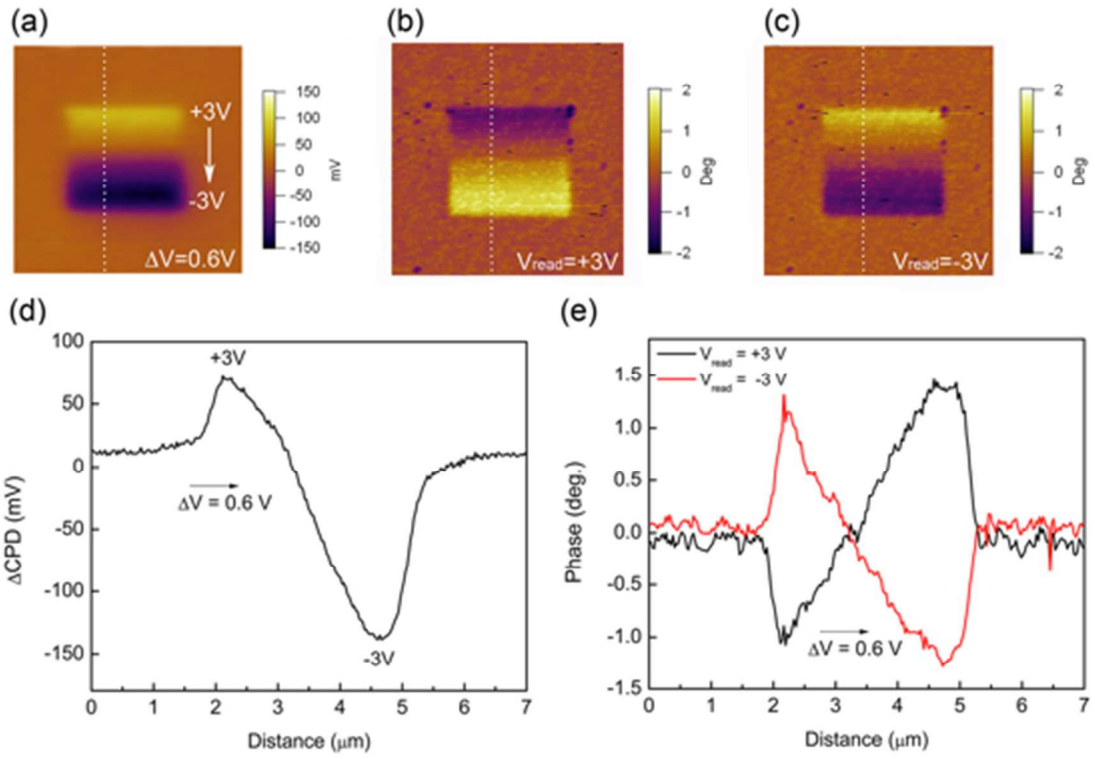

Fig. 7